Article

Laser Machining at High ~PW/cm2 Intensity and High Throughput

Nan Zheng , Ričardas Buividas * , Hsin-Hui Huang , Dominyka Stonyte , Suresh Palanisamy , Tomas Katkus , Maciej Kretkowski , Paul R. Stoddart , Saulius Juodkazis *

Posted Date: 3 June 2024

doi: 10.20944/preprints202406.0038.v1

Keywords: laser machining; ultra-short laser pulses; 3D printing

Article

Laser Machining at High ∼PW/cm^2 Intensity and High Throughput

Nan Zheng [1,#], Ričardas Buividas [1,2#*], Hsin-Hui Huang [1,*] Dominyka Stonytė [3], Suresh Palanisamy [4], Tomas Katkus [1], Maciej Kretkowski [5], Paul R. Stoddart [6] and Saulius Juodkazis [1,3,7]

[1] Optical Sciences Centre, ARC Training Centre in Surface Engineering for Advanced Materials (SEAM), Swinburne University of Technology, Hawthorn, Victoria 3122, Australia; rbuividas@swin.edu.au; nzheng@swin.edu.au; hsinhuihuang@swin.edu.au
[2] Quoba Systems Pty. Ltd., 26-28 Roberna St., Moorabbin VIC 3189, Australia;
[3] Laser Research Center, Physics Faculty, Vilnius University, Saulėtekio Ave. 10, 10223 Vilnius, Lithuania; dominyka.stonyte@ff.vu.lt
[4] Department of Mechanical Engineering and Product Design Engineering, Swinburne University of Technology, Hawthorn, Victoria 3122, Australia; spalanisamy@swin.edu.au
[5] Research Institute of Green Science and Technology, Shizuoka University, 432-8011, Hamamatsu Campus, Japan; kretkowski.maciej@shizuoka.ac.jp
[6] Department of Engineering Technologies, Swinburne University of Technology, Hawthorn, Victoria 3122, Australia; pstoddart@swin.edu.au
[7] WRH Program International Research Frontiers Initiative (IRFI) Tokyo Institute of Technology, Nagatsuta-cho, Midori-ku, Yokohama, Kanagawa 226-8503 Japan;
* Correspondence: R.B., ricardas.buividas@quobasystems.com.au; H-H.H. hsinhuihuang@swin.edu.au
‡ # R.B and N.Z. contributed equally to this work.

Abstract: Laser machining by ultra-short (sub-ps) pulses at high intensity offers high precision, high throughput in terms of area or volume per unit time, and flexibility to adapt processing protocols to different materials on the same workpiece. Here we consider the challenge of optimization for high throughput: how to use the maximum available laser power and larger focal spots for larger ablation volumes by implementing a fast scan. This implies the use of high-intensity pulses approaching ∼PW/cm^2 at the threshold where tunnelling ionization starts to contribute to overall ionization. A custom laser micromachining setup was developed and built to enable high speed, large area processing and easy system reconfiguration for different tasks. The main components include laser, stages, scanners, control system, and software. Machining of metals such as Cu, Al, or stainless steel, and fused silica surfaces at high-fluence and high-exposure doses at high scan speeds up to 3 m/s were tested for the fluence scaling of ablation volume, which was found to be linear. Modified surfaces are color-classified for their appearance, which is dependent on surface roughness and chemical modification. Such colour-coding can be used as a feedback parameter for industrial process control.

Keywords: laser machining; ultra-short laser pulses; 3D printing

1. Introduction

Tools have defined technical advancement throughout human history. They should provide the required virtues for particular tasks, and very often for material processing, where they should have high resolution and high throughput of area or volume processing. However, resolution and throughput are usually considered a trade-off [1], which is known as Tennant's law in the fields of optical and related lithographies [2], and ultrafast laser processing [3]. It becomes an optimization task to simultaneously achieve a specific resolution required for an application and to enhance throughput, usually through power scaling of the writing source (laser, electron beam, or ion beam). In optical lithography for microelectronic applications, high throughput was achieved via large area projection systems [4–7], while resolution was gained by using shorter wavelengths [8–11]. However, these large-area processing tools are naturally losing flexibility to be adapted for different processes and are increasingly expensive due to the requirement for highly uniform exposure conditions over larger areas. Also, the multi-step fabrication processes in microelectronics create an additional challenge for overall throughput.

The recent decade of advances in 3D printing has stemmed from flexibility, on-demand fabrication, and prototyping capabilities which are well aligned with the relatively small footprint of tools/printers and low ownership and maintenance costs. One common virtue of 3D printing approaches based on the use of light, fluidics, moulding, embossing, etc., is the direct writing approach. While this sacrifices the productivity gains of large-area projection tools, it benefits from the ability to deliver the required exposure dose of energy/material for building a workpiece with tailored properties on the surface and inside the volume. When the depth of energy deposition becomes important for volume-per-time modification (rather than the saturation of thin film "resist" exposure), laser machining is a very appealing approach [12].

Laser 3D processing of materials by the direct write approach is one of the most rapidly developing computer numerical control (CNC) machining methods, especially, when ultra-short pulsed lasers are used [13]. This leads to precise laser machining applications such as nano-scaled gratings [14,15] and nano-alloys [16]. Uniquely for sub-ps lasers, the pulse energy can be delivered and deposited faster than the material response: it takes ~ 10 ps for energy transfer from the absorbing electronic sub-system of solid/liquid/gaseous phases to the atomic/molecular/ionic core sub-system. Subsequent hydrodynamic movement and phase transitions occur on time scales from tens-of-ps to microseconds. With a burst mode, where fs-pulses can be bunched into bursts with time separation corresponding to even higher MHz-GHz frequencies while keeping low frequencies of $<$MHz between the bursts, the fastest material removal rates ~ 3 mm^3/min become accessible and are comparable with mechanical CNC machining [17]. Similar arguments about using different energy deposition modes for high throughput modification of refractive index n in transparent materials predict that energy-per-volume is more effective than the power of exposure for a large change of n [18].

A particular aim of this study was to test the possibility of assembling the laser, stages, scanners, and 3D CNC machining software into a functional unit and to demonstrate the feasibility of laser ablation/patterning of large volumes/surfaces. Using the resulting setup, we apply high-pulse intensity/fluence per pulse [W/cm^2 and J/cm^2] with different total exposure doses up to 0.3 kJ/cm^2 (per focal diameter) for laser machining of strongly reflective metals Al, Cu, and stainless steel, based on a laser with 1030 nm wavelength and 200 fs pulses at 0.1 MHz repetition rate when thermal accumulation is not dominant. The ablated volume reached significant removal rates $V_a \sim 10^4$ μm^3 at high beam travel speeds of ~ 1 m/s and scaled linearly with the fluence-per-pulse, i.e. $V_a \propto F_p^\gamma$ with $\gamma \approx 1$. The irradiance used for laser machining ~ 0.2 PW/cm^2 was approaching conditions where tunnelling ionisation becomes important (above 1 PW/cm^2; see, Appendix Sec. A). As compared with avalanche and multi-photon ionizations, which are dominant at 1-10 TW/cm^2, tunnelling ionization is of interest for more deterministic material machining due to the possibility of reaching higher precision, resolution, and polarization controlled chemical bond breaking.

2. Experimental: Setup and Materials

2.1. Assembly of fs-Laser Machining Setup

Multi-axis femtosecond laser CNC micro-machining system (Quoba Systems, Figure 1(a)) includes a high-power femtosecond laser, high-speed galvanometer scanner, 5-axis sample positioning stages, system control, and software. The laser: 80 W Carbide (Light Conversion), wavelength of choice $\lambda = 1030, 515, 343$ nm, pulse duration $t_p = 200$ fs, maximum pulse energy of 0.8 mJ, maximum repetition rate $f = 2$ MHz and tunable GHz and MHz burst with burst-in-burst (bi-burst) capability. In burst mode, the output consists of pulse packets instead of single pulses, where each packet consists of a certain number of equally separated pulses. MHz-Burst contains up to 10 pulses with a 15 ns period and GHz-Burst contains up to 10 pulses with a 440 ps period. Intra-burst amplitude slope can also be adjusted. Switching and adjusting bi-burst mode is fully automated. Carbide laser comes with a fast energy control (FEC) capability, which allows changing the energy of each laser pulse at MHz repetition rate. Switching between linear and circular polarisation is also implemented across different wavelengths.

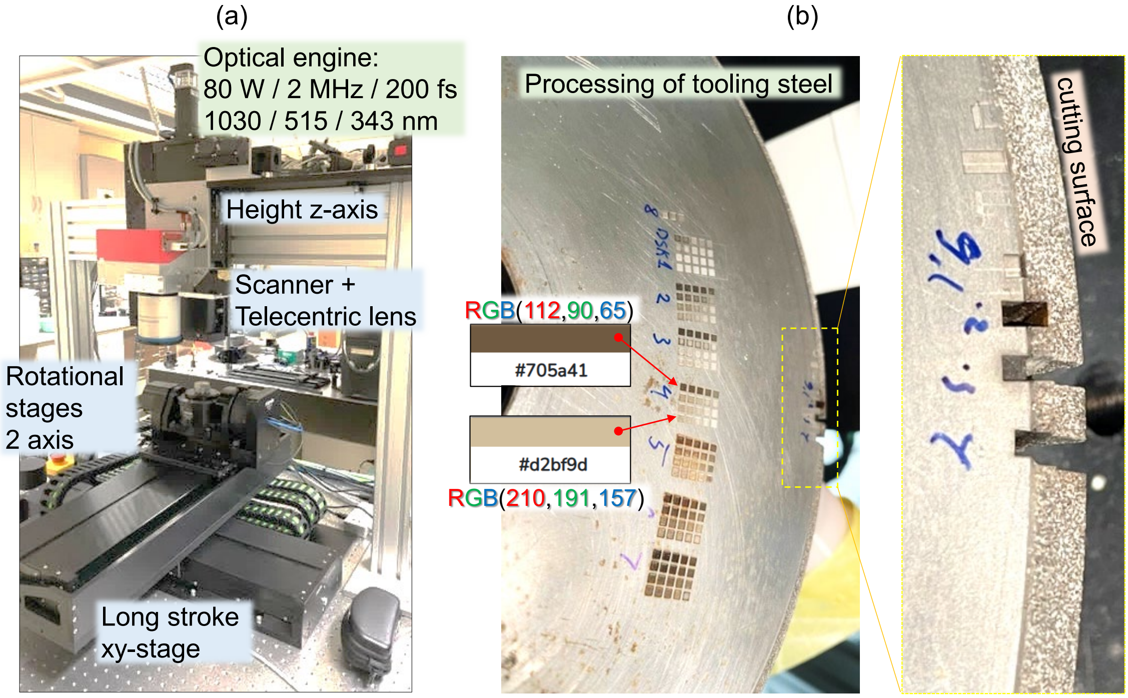

Figure 1. (a) Laser CNC machining assembly: laser, stages, and beam scanners for typical fs-laser setup. (b) Laser machining of tooling steel and material cutting section where abrasive micro-sharp materials are bound to the wheel shown at different resolutions (see text for parameter study). The correspondence between the fabrication parameter space can be mapped onto colour as a colour-to-condition map (see, HEX colour codes on the two selected matrix patches and their RGB values in (b); made with online tool https://html-color.codes/); ablation matrices for parameter dependencies can be explored: power/fluence vs. pulse density, repetition rate vs. scan speed, etc. defining the exposure dose.

The telecentric fused-silica F-theta lens (Jenoptic, JENar) with $F = 160$ mm focal length was used with a galvanometer scanner (Raylase, SUPERSCAN IV). The laser beam diameter $D = 5$ mm. This defines F-number $F_\# = F/D = 32$ and numerical aperture $NA = 1/(2F_\#) = 0.0156$. Theoretical diameter at focus $2r = \frac{4\lambda}{\pi}F_\# = 42\ \mu$m. The depth-of-focus, $DoF = \frac{8\lambda}{\pi}F_\#^2 = 2.69$ mm for $\lambda = 1030$ nm; the axial extent of the pulse $ct_p = 60\ \mu$m. With the most conservative estimate of the laser beam quality factor $M^2 = 1.2$ (measured value $M^2 = 1.1$) the beam diameter at focus becomes 50.5 μm and the depth-of-focus $DoF = 3.87$. Specifications of F-theta lens focusing for the input beam at the used conditions give an estimate of $2r = 60\ \mu$m for the entire scanning field of 50x50 mm. This was used for the calculation of fluence and intensity. Due to long DoF, multiple scans $N_{sc} = 1 - 10$ were used to ablate deeper structures without a change of focusing depth. A change of scan direction was used between subsequent layers. Galvanometer scanners were equipped with dual-coating mirrors to accommodate for 1030 and 515 nm wavelengths.

High precision, direct drive stages (Standa) with non-contact optical encoders ensure high positioning accuracy: 0.5 μm bidirectional repeatability, 1 μm absolute accuracy over the whole travel area of 400 × 400 mm. Maximum acceleration and speed are 2 g and 2 m/s respectively. Stages were used for translating samples beyond the scanning field of a galvanometer scanner (50 × 50 mm in this case). The galvanometer scanner was mounted on a 200 mm travel Z stage with a high 20 kg vertical load capacity, and similar positioning accuracy specifications as XY stages. System controllers (Polaris) were used to synchronize all axes with the laser providing an infinite field of view (IFOV) capability, which splits motions task between stages and scanners optimizing scanning speed and accuracy and eliminating stitching errors.

The system is controlled using a very capable and flexible software package (Direct Machining Control-DMC), which simplifies laser machining design providing a user-friendly interface and ability to import various format fabrication tasks and also generate very complex machining paths without any G-code or other programming knowledge. DMC also integrates machine vision capability and provides automated galvo scanner field calibration.

The system is very modular and allows easy modifications to suit different fabrication requirements. Two high-precision rotational axes are available for a full 5-axis fabrication capability. Software and controllers are designed to control all 7 axes in real time and can accommodate up to 32 axes in total. The system also allows simple integration of high-NA objectives for high resolution (down to sub μm) fabrication and Bessel beam setup integration for high speed cutting of transparent materials.

2.2. Ablation and Structural Characterisation

Focusing and processing conditions: the beam diameter on the surface $2r = 60$ μm (nominal, without a telescope before F-theta lens) and twice smaller with a beam expander, depth of focus $DoF \approx 2.7$ mm (nominal), scan speed for linear beam travel $v_{sc} = 100 - 1$ mm/s (along x-direction), which defines the number of pulses per diameter from 60 to 6000 at $f = 0.1$ MHz (usual fabrication sequence was at a constant density of pulses per length of scan). Hatching between neighbouring lines was chosen slightly smaller than the focal diameter and was $\Delta y = 50$ μm. The maximum fluence per pulse was $F_p = 28.3$ J/cm^2 and consequently average intensity $I_p = 0.14$ PW/cm^2.

A Geiger counter (Radhound with an SS315 probe) sensitivity to hard X-rays above an energy level of 20 keV was used to monitor the emission of bremsstrahlung background. The background noise from the lab environment was 25 ± 5 counts per min (cpm). Shielding the direct view of the fabrication location on a workpiece with a sub-mm thick Al-sheet was enough to reduce the X-ray counts back down to background level. RDS-32 monitor was used to determine radiation dose in μSv ($\sim$ 20 cm from fabrication site) and was always at the background level for the highest power and pulse-to-pulse overlap (6000 pulses per diameter of 60 μm).

Optical microscopy (Nikon Optiphot-Pol.) and profilometer (Bruker) were used to image laser machined regions and to determine the depth, which was evaluated with a precision of ~ 0.1 μm using a high numerical aperture objective $NA = 0.4 - 0.9$ lenses.

2.3. Material Properties

Light-matter interaction is defined by the permittivity, a square of the complex refractive index $\epsilon_1 + i\epsilon_2 \equiv (n + i\kappa)^2 = (n^2 - \kappa^2) + i2n\kappa$ of material at the wavelength of excitation (see Sec. B for other definition of the permittivity of metals). Herein we collect material parameters relevant to the analysis (Sec. 3). Energy values for good metals: electron work function for Cu $w_e = 5.10$ eV $\langle 100 \rangle$ orientation, 4.48 eV $\langle 110 \rangle$, 4.94 eV $\langle 111 \rangle$ and for Al 4.20; 4,06; 4.26 eV ($\langle 100 \rangle; \langle 110 \rangle; \langle 111 \rangle$). For stainless steels, $w_e = 4.08 - 4.19$ eV [19]. The refractive index at 1030 nm: $n + i\kappa = 1.4033 + i9.8532$ (Al: absorption coefficient $\alpha = 1.2021 \times 10^6$ cm^{-1}), $0.33769 + i6.7731$ (Cu: $\alpha = 8.2634 \times 10^5$ cm^{-1}), $n = 2.9421 + i3.9094$ and $\alpha = 4.7696 \times 10^5$ cm^{-1} for Fe (the main component of stainless steel).

The molar enthalpy of vaporisation (and atomisation) of Cu is 300 kJ/mol (338 kJ/mol) and similar values for Al 293 kJ/mol (326 kJ/mol). Solid density of Cu $\rho_{Cu} = 8920$ kg.m^{-3} (molar volume 7.11 cm^3 and atomic weight $M_{Cu} = 63.546$ g) and that of Al $\rho_{Al} = 2700$ kg.m^{-3} (molar volume $\frac{M_{Al}}{\rho_{Al}} = 10$ cm^3 where atomic weight $M_{Al} = 26.98154$ g).

3. Framework for Analysis and Bench-Marking of Ablation Efficiency

Normalisation of ablation rate for the volume removal per pulse energy (for a photon) and the number of pulses (per pulse), e.g., μm^3/μJ/pulse can be introduced to compare the ablation efficiencies of different fabrication methods and conditions.

The material removal for dielectric by fs-laser was matched to mechanical CNC machining rate in a burst mode for the dental tissue ablation by ~ 800 fs laser pulses [17] reaching $V_r = 5\times 10^7~\mu\mathrm{m}^3/\mathrm{s}$ (or $\sim 3~\mathrm{mm}^3/\mathrm{min}$) with $N_{ib} = 25$ pulses (in a burst) of $E_p = 4~\mu\mathrm{J}/\mathrm{pulse}$ energy at $f_{ib} = 1.7$ GHz (in a burst) and separation between bursts was at $f_{bb} = 1$ kHz rate. At those conditions, good final quality of the ablated cavity was achieved via proper thermal management (no cracks were formed). The measure of ablation-volume-per-single-pulse is estimated as a removal rate per pulse and normalized to its energy as $\eta_p = V_r/(f_{bb}N_bE_p)$ $[\mu\mathrm{m}^3/\mu\mathrm{J}/\mathrm{pulse}]$. This estimate is still dependent on the in-a-burst frequency f_{ib}. The η_p was increasing for the smaller E_p when f_{ib} is large in a nonlinear way due to thermal accumulation. For the burst removal of dental tissue, the efficiency per pulse was $\eta_p = 500~\mu\mathrm{m}^3/\mu\mathrm{J}/\mathrm{pulse}$. This example shows the ablation efficiency of a material of complex composition using single and burst modes of laser irradiation.

3.1. Energy Deposition Depth: Localisation Mechanism

The common phenomenon of different ablation modes by ultra-short laser pulses with and without bursts is a shallow energy deposition. It is responsible for the most efficient material removal rate for the efficiencies of volume-per-time and volume-per-photon. It is instructive to analyse energy deposition at the ablation threshold for metals and dielectric materials for the pulse fluence by the Gamaly model [20]:

$$F_{th}^{(m)} = \frac{3}{8}(\epsilon_b + w_e)\frac{\lambda n_e}{2\pi}, \quad F_{th}^{(d)} = \frac{3}{4}(\epsilon_b + J_i)\frac{l_s n_e}{A}, \tag{1}$$

where ϵ_b is the binding energy or enthalpy of vaporization, J_i is the ionization potential, w_e is the electron work function (escape energy from a metal), $l_s = c/(\omega\kappa) \equiv \lambda/(2\pi\kappa)$ is the absorption depth (the skin depth) in the plasma with electron density n_e and refractive index $n^* = n + i\kappa$ with c, ω being the speed and cyclic frequency of light, respectively, A is the absorption coefficient (for good metals $A \approx \frac{2\omega l_s}{c}$). At high intensity, the pulse can exceed the ionization threshold and the first ionization is completed (before the end of the pulse), at which the number density of free electrons saturates at the level $n_e \approx n_a$, where n_a is the number density of atoms in the target material.

For ablation of dielectrics and semiconductors, which are ionised during the fs-pulse, a metal-like reflective plasma has $A \approx 0.5$, i.e., the half of light is absorbed by the strongly excited material. Exact absorbed portion $A = 1 - R$ can be precisely calculated from the refractive index n^* for the excited material as $A = 4n/[(n+1)^2 + \kappa^2]$). The most direct improvement of efficient (shallow) light energy deposition is achieved by the use of a shorter wavelength since $l_s \propto \lambda$. Interestingly, the ablation threshold of metals (Eqn. 1) also scales with wavelength $F_{th}^{(m)} \propto \lambda$ [20].

Equations 1 are based on the required energy budget to evaporate material ϵ_b and to ionize it: w_e for metals and J_i for dielectrics. For metals, the electron work function enters the energy budget required to free electrons from metal. The absorbed energy required for ablation is deposited into the skin depth l_s into excited material (dielectric or metal) with electron density n_e and the portion of light absorption is defined by A ($A = 0.5$ for the 50% absorbance). These ablation thresholds are confirmed by experiments for metals and dielectrics [20].

3.2. Ablation Rate

The theoretical limit of ablation rate per pulse is reached when the absorbed energy $(1-R)E_p$ ($T = 0$ for the energy balance $R + T + A = 1$) is equal to the enthalpy of vaporisation ϵ_b (binding, cohesive, atomisation energy) in the volume where it is deposited. Since light absorption follows an exponentially decaying dependence via Beer-Lambert law, the shallow deposition into skin depth $l_s = 1/\alpha$ takes place for the most efficient material ablation. Such ablation is taking place by evaporation only as follows from the chosen energy balance. The ablation when ionisation of material and plasma formation is taking place requires a higher energy budget $(\epsilon_b + J_i)$ (Eqn. 1).

The temperature of electrons in the skin depth is $T_e = (1-R)F_p/(l_s c_e n_0)$ [20], where F_p is the fluence per pulse and $c_e \sim 3/2$ is the electron specific heat, which acquires the value of 3/2 of the ideal gas after full ionization of material. This energy pool delivered to electrons acts as an energy reservoir for ablation after ultra-short laser pulse, e.g., T_e reaching ~ 2 keV in metal and silicon drilling [21]. The maximum material removed by a single pulse can be estimated from energy conservation [20]:

$$V_{max} = (1 - R)E_p/(n_0 E_{at}/N_a), \tag{2}$$

n_0 is the atomic number density of the material, E_{at} [J/mol] is the molar enthalpy of atomization and the reflection coefficient is R.

However, the practical ablation rates by vaporisation in terms of removed volume V_r [μm^3/s] will not be the fastest, however, the most efficient in terms of deposited light energy. Kinetic factors are very important and are qualitatively discussed here for different ablation conditions.

3.3. Power Scaling Is for Energy Deposition Per Volume

Interestingly, the ablation efficiency of the burst ablation of dental tissue (dielectric) scales as $\eta_p \propto E_p^2$ [17] while in single pulse ablation, it is a linear dependence and it was extending all the tested pulse energy values for case of direct absorption $\eta_p \propto E_p$ [12]. Such difference can be explained by the density of absorbed energy, which scales as $W_{abs}[\mathrm{W/cm^3}] = 2AF_p/l_{abs} \propto \frac{n_e}{n_{cr}}F_p$ [20,22], where $n_e \propto F_p$ is photo-excited electron density (which is also proportional to the fluence per pulse F_p) and $n_{cr} = \frac{\epsilon_0 m_e}{e^2}\omega^2$ is the critical electron density where m_e, e are the mass and charge of electron and $\omega = 2\pi c/\lambda$ is the cyclic frequency of light, ϵ_0 is the permittivity of vacuum and l_{abs} is axial extent of energy deposition along beam propagation ($n_{cr} = 9.48 \times 10^{21}$ cm^{-3} at 343 nm wavelength [12] and 1.04×10^{21} cm^{-3} for 1035 nm used in burst-ablation).

For the conditions when electron density $n_e < n_{cr}$ the absorbed energy density follows a nonlinear $W_{abs}(I_p) \propto n_e(I_p) \times F_p/n_{cr}$ dependence on pulse intensity (irradiance) I_p, while it becomes linear when plasma of the critical density $n_e = n_{cr}$ is reached. The cavitation ablation rate [12] was following the third power law $\gamma = 3$ for silica when absorption mechanism was two-photon. This corresponds to two-photon absorption in electron excitation $n_e \propto I_p^2$, hence the absorbed energy density in the volume, which is proportional to the ablated volume $W_{abs} \propto F_p^3$; the pulse energy, fluence and irradiance are all proportional to each other $E_p \propto F_p \propto I_p$. In the case of burst-ablation of dental tissue, the ablation rate was following $\propto F_p^2$ [17], which can be explained by the linear absorption $\gamma = 1$ for $n_e \propto I_p$. For metals when absorption of the laser pulse is not increasing the electron density, which is close to n_{cr}, a linear scaling with $\gamma = 1$ is expected as was confirmed in this study.

4. Results

We aimed to use the maximum available laser power of $P = 80$ W with pulse energy $E_p = 0.8$ mJ per pulse at the repetition rate $f = 0.1 - 1$ MHz to maximize the use of the available light energy. The scan speed and focus were tuned for the required quality of the processed surface (smooth or rough), and the depth of ablated structures (hence removed volume V_a ~mm^3/min). Typical ablation threshold of metals by pulses of $\lambda \sim 1$ μm and pulse duration $t_p = 200$ fs was only 0.1 J/cm^2, 0.2 J/cm^2 for Silicon and ~ 2 J/cm^2 for wide bandgap glass and crystal (fused silica and Al_2O_3).

Figure 2(a) shows typical samples of Al and Cu which were ablated at an extensive range of conditions: from full power of 80 W corresponding to pulse energy $E_p = 800$ μJ down to 8 μJ. The repetition rate was set $f = 0.1$ MHz and linear travel speed of 60 μm focal spot was at $v_{sc} = 0.5, 1, 2, 3$ m/s corresponding to the pulse to pulse separation $\Delta_{x,y} \approx 7, 14, 28, 42$ μm; these are the measured separations determined from ablation pattern and are slightly larger from the set conditions due to very fast scan rates, which were focus of this study. The same spacing was used in x- and y-directions for the most uniform material removal.

The depth, width, and volume ablated using single and ten times repeated scans are shown in Figure 2(b,c,d), respectively. The log-log presentation reveals the scaling dependencies. The depth evolved as $\propto F_p^{0.5}$, which indicates a heat diffusion process. A strong difference in depth for one and ten passes was observed. However, for the width, single and multi-pass structures converged and showed $\gamma = 1$ dependence. For the ablated volume, a close to linear dependence was observed for both Al and Cu. Since the critical density n_{cr} for 1030 nm is smaller than the electron density in those metals n_e, the linear scaling of ablated volume with is expected as shown above.

When the scanning speed was large enough to separate single pulses, SEM images revealed a nano-texture formation even for single pulses at low and high pulse fluence (Figure 4). The surface of Al and Cu cupons had a micro-texture which was enhanced by ablation. This could be contributing to lower reflectivity of the laser-treated regions and favours stronger energy deposition in subsequent passes. This tendency can be inferred from scaling $\gamma > 1$ in Figure 3.

Figure 4 shows typical single pulse ablation sites on Al and Cu characterised by SEM. The surface of used coupons had micron-scale structures due to mechanical cutting. Those structures affected light distribution and consequently ablation. They are reminiscent of typical ablation ripples, which have a period (0.8-1)λ for absorbing samples under multi-pulse exposure, however here they were produced by single pulse exposure at high or low pulse energy. Interestingly, the affected region was larger than the directly exposed (I_{max}/e^2-level) for the highest pulse energy. Since the threshold of laser ablation fluence is only $\sim$ 0.1 J/cm^2, low-intensity regions of the laser beam can already be delivering the required ablation fluence. The threshold of ablation is dependent on the energy distribution of the surface atoms and it was shown to require time to be established, i.e., the high-energy side of the Maxwellian velocity distribution has to be established before evaporation from the surface can take place [24]. Ablation in vacuum showed approximately the twice higher ablation threshold [24] and is linked to slower thermalisation when there is no ambient air. It would be useful to measure the ablation threshold at low pressure $\sim 10^{-3}$ bar ($\sim 10^2$ Pa) for the conditions used in this study, which was performed in ambient air. The same high average power ablation as used for metals was applied to scan lines on fused silica (Figure 5). Analysis of ablation width vs pulse fluence was carried out using the Liu method [23]. Single pulse $N = 1$ ablation threshold for silica is $F_{th}(1) = 2$ J/cm^2. For a linear scan with $\Delta x = 20$ μm translation step between laser pulses a smaller threshold was observed $F_{th}(N = 3) \approx 0.8$ J/cm^2. This can be explained by the accumulation of defects which cause increasingly stronger absorption for N number of pulses. Phenomenologically it is defined by the accumulation exponent γ_a: $F_{th}(N) = F_{th}(1) \times N^{\gamma_a - 1}$, where $\gamma_a = 1$ corresponds to absence of accumulation. Accumulation was present in the case of $N \approx 3$ for silica. The change of slope of the $w^2 \propto F_p$ dependence (Figure 5) was approximately when the width of the ablated groove became larger than the focal diameter. In this case, the absorbed energy spread by heat diffusion and was high enough to facilitate material removal by either of the ablation mechanisms of explosive boiling, evaporation, or ionisation. The threshold of ablation at those conditions was $\sim$ 9 J/cm^2. This threshold is close to a factor of $e^1 = 2.718$ larger than the single pulse threshold of 2 J/cm^2 typical for glasses [25]. The optical energy deposition and absorption are scaling as $e^2 = 7.39$ for intensity according to Beer-Lambert's law. It is usually applied to the depth profile of energy deposition in ablation studies [26].

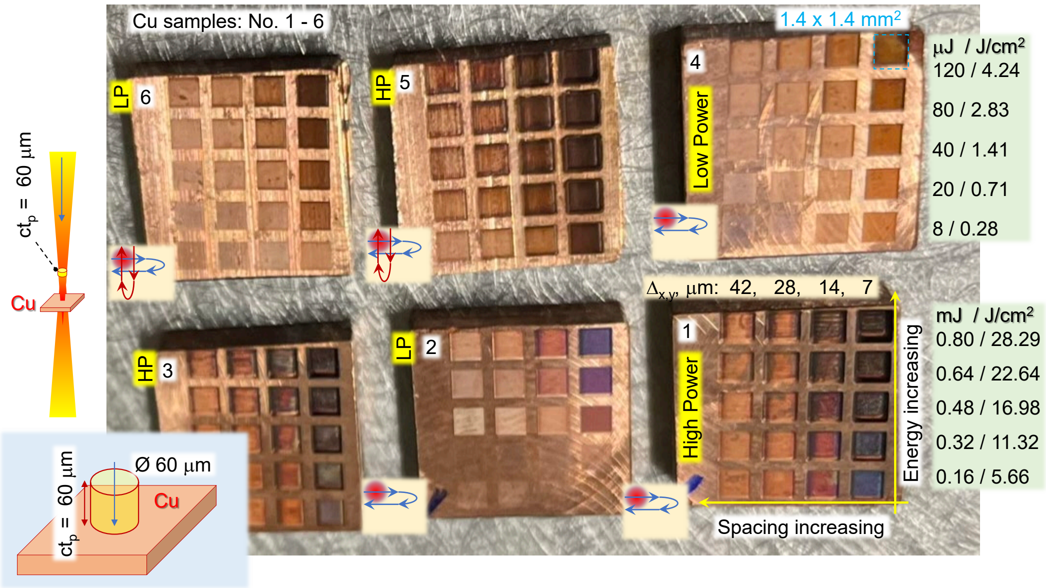

Figure 2. Typical 1×1 cm^2 coupon-samples (Cu) used for determination ablation rates. Samples are not polished. High and low power ranges were used to explore the different surface roughness and material removal rates of ablated surfaces, see, pulse energy E_p and fluence F_p [J/cm^2]. F-theta lens had focal diameter on the sample $2r = 60\ \mu$m, depth of focus $DoF = 2.7$ mm, field of scan 50×50 mm^2, and axial pulse extent of $ct_p = 60\ \mu$m for pulse duration of $t_p = 200$ fs. The melting temperature of Cu is 1085°C, evaporation/boiling 2595°C. For samples No. 1, 2 the focal spot was placed 6 mm deeper along beam propagation from the top surface of the sample. Hatching passes in x-/y-directions are schematically shown; the total number of passes was always 10.

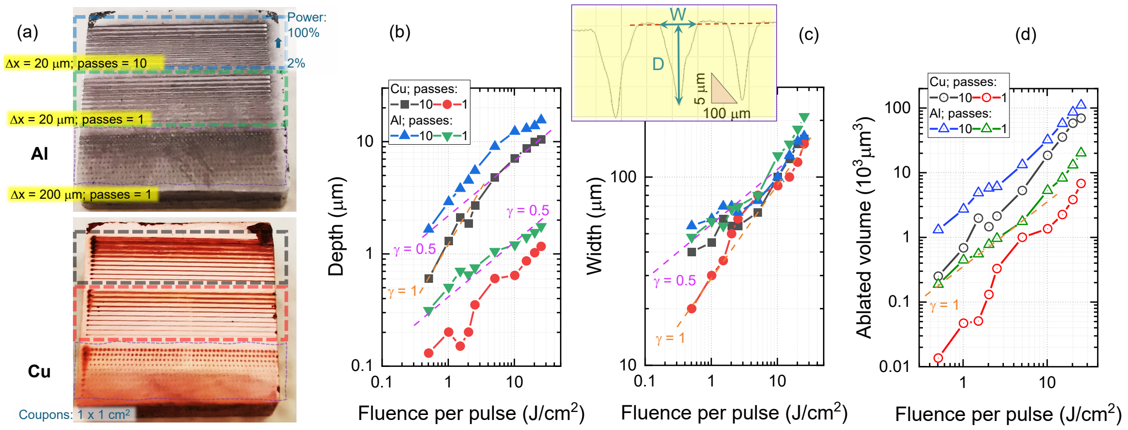

Figure 3. (a) Ablated lines at different pulse energies (powers) at 1 and 10 repeated passes on Cu and Al 1×1 cm^2 coupons. Depth D (b) and width W (c) of the ablated line vs. fluence per pulse; 1030 nm/200 fs/0.1 MHz at scanning speed corresponding to in-line separation between pulses $\Delta x = 20\ \mu$m and 200 μm (single pulses regime Figure 4) and distance between lines 0.25 mm. The inset shows the cross-section of optical profilometer. (d) Ablated volume of cone $V = \pi D[W/2]^2/3$ at different fluence per pulse (in terms of average power from 2% to 100%). The slope of power dependencies $D, W, V \propto F_p^{\gamma}$ correspond to the linear $\gamma = 1$ and diffusional $\gamma = 0.5$.

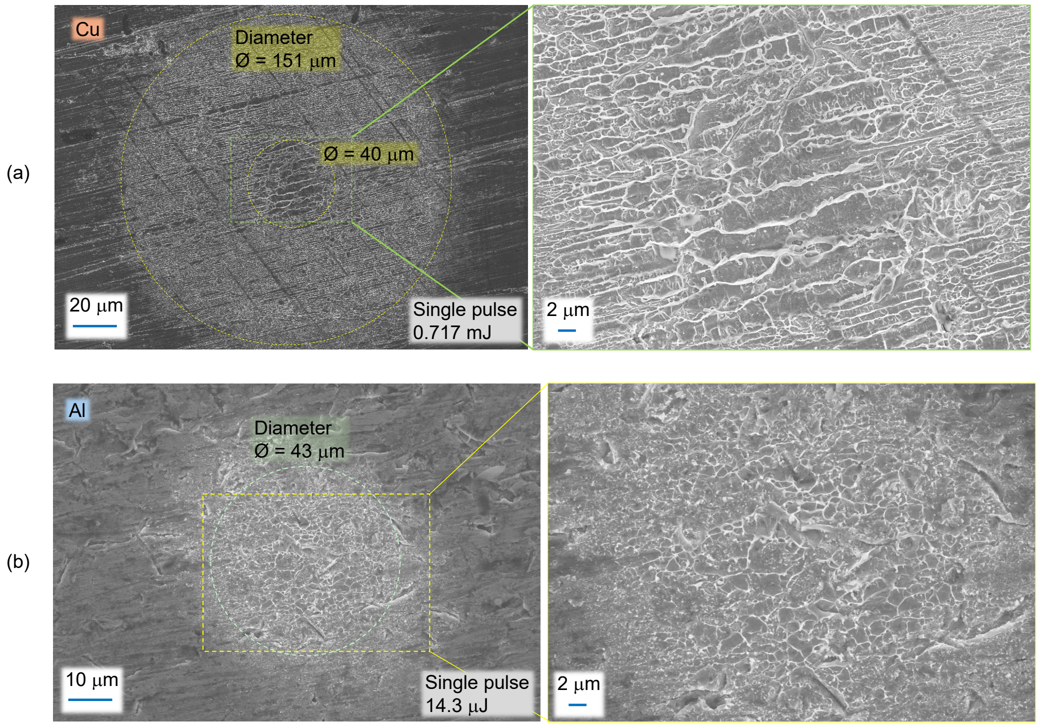

Figure 4. (a) SEM images of single pulse ablation sites (see Figure 3(a)) at high and low pulse energies on coupons of Cu and Al, respectively. The focal spot size is $\sim 60\ \mu$m.

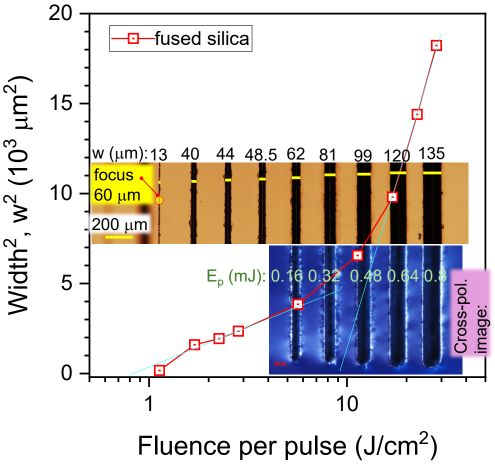

Figure 5. The width vs pulse fluence $w^2 \propto F_p$ [23] for 1030 nm/200 fs/0.1 MHz irradiation of silica glass at scanning speed corresponding to the in-line separation between pulses $\Delta x = 20\ \mu$m. The focal spot size is $\sim 60\ \mu$m. Insets show optical transmission and cross-polarised images of the ablated trenches.

4.1. X-ray emission

X-ray emission was monitored and observed during laser fabrication with different pulse overlaps. In all cases, the same 100 kHz repetition rate, 200 fs pulse duration and 0.8 mJ energy were used. Spot size 60 μm and fluence 28 J/cm^2. The X-ray emission was already 6 times above the background at 150 cpm (counts per minute) when the gap between pulses is at 1 μm, 60 pulse overlap per focal spot along the scan. The emission reaches the highest level of $\sim 1.5 \times 10^5$ cpm when the gap between pulses was reduced to 0.1 μm, i.e. the overlap of 600 pulses per focal spot. However, the emission drops down to $\sim$ 1850 cpm when the gap between pulses becomes even smaller at 0.01 μm or the overlap of 6×10^3. This drop is related to a larger volume removed from the focal volume by ablation and reduced amount of material affected, hence less bremsstrahlung radiation.

5. Discussion

Color appearance of the ablated matrices which are typically used for optimisation of two independent parameters of surface processing, while keeping others constant, can be digitized into HEX codes (or RGB values) as shown in Figure 1(b) for two segments.

Parameter information represented by colour has the advantage of being both human and machine-readable. However, in an RGB colour system, the colour information is being acquired in a device-dependent manner. Using cameras operating in RGB colour space would require colour calibration for the particular illumination conditions for the best colour acquisition fidelity. Likewise, the reproduction of colour on a display also has to be calibrated. Calibrated imaging systems can be very powerful and efficient in encoding various parameters, even more so in the trichromatic XYZ colour space [27] which is device-independent and captures colours within the full vision gamut [28]. XYZ colour space is much more accurate and can be also re-calculated (with loss) to RGB, sRGB, L*a*b* (lossless) and other high-fidelity colour systems.

In case of analysis of the ablation matrices, the choice of the colour acquisition instrument (camera vs colourimeter) is dictated by the required precision of colour identification. The colour change that results from varying the ablation parameters can also be used for aesthetic and functional purposes. In case of materials, where coatings may not be desirable (like stainless steel or copper) a typical silkscreen layer used for marking the product can be replaced by ablation marks with colours of choice induced by chosen laser parameters. Typical mechanical or laser engraving is very limited in that respect and usually requires additional setup in the production process. With laser machining, the simplification of the processing setup may be a big advantage in production costs. Moreover, using materials that exhibit colour change induced either electrically [29] or via mechanical stress [30] can open up a wide range of applications for laser-machined sensors/devices working on purely mechanical principles, low-energy consumption strain indicators, cutting tools with a level of wear indicated by colour change and many other applications. In addition to the above, recent developments in AI technology coupled with increasing throughput allow for 5-axis laser machining to be introduced to the market with much more user-friendly software packages with learning curves much less steep than in conventional cutting. With the non-contact approach to processing materials with lasers, thin-walled and fragile components can be manufactured with great precision at relatively low cost which benefits many fields of applications, most notably single-use biomedical components, surgical tools and health care equipment.

Colourimetric quantisation of laser-processed regions on metals discussed above can have other applications in laser-processed regions inside the volume of transparent materials (Figure A2). In this case, laser-damaged regions show stress-induced birefringence for a circularly polarized light. This polychromatic polarization microscope (PPM) imaging is promising for colour analysis under white light illumination.

The black appearance of surface has another application potential at IR spectral range. Such surfaces have high emissivity $\epsilon \to 1$ according to the Kirchhoff's law $\epsilon \equiv \alpha = 1 - R$ [31], where R is the reflectance, and such emissivity improvement has been demonstrated on aluminium [32], sapphire [33] and Metal-on-Insulator metasurfaces [34]. Metals are usually reflective but not emissive. Formation of black metal surfaces (see Al surfaces in the insets of Figure A1(b,c)) is inviting for their characterisation at IR-THz spectral range and possible use for radiative cooling at 7-14 μm spectral window of atmospheric transmission.

6. Conclusions and Outlook

Normalisation to the number of pulses and pulse energy (number of photons) is a useful tool to compare very different ablation modes with high-frequency bursts as well as single pulses at different pulse overlapping modes during laser machining. The accumulation exponent of the ablation threshold is a useful parameter to assess the contribution of accumulation. The ablated volume of Al and Cu was found scaling linearly with pulse fluence at high-intensity conditions.

The ablation thresholds are defined by the fundamental material parameters such as binding energy, electron ionisation potential and work function, the skin depth electron density (original for metals and photo-excited for dielectrics) and are dependent on the ambient pressure. The permittivity $\varepsilon = \tilde{n}^2$ of material defines the energy deposition via the skin depth $l_s \propto \kappa$. This shows importance of energy-per-volume $\mathrm{J/cm^3}$ in analysis of ablation and material removal for the defined fluence per pulse $\mathrm{J/cm^2}$. The absolute limit of material removal per pulse energy is based on energy conservation (Eqn. 2).

Ablation of lower melting temperature metal such as Al, showed micro-structure with feature sizes comparable with the dimensions of the focal spot. Black surfaces were formed on usually reflective Al at visible spectral range. Feature sizes of tens-of-micrometers make such surfaces anti-reflective and, hence, emissive at the longer IR-to-THz spectral range and will be investigated in the follow-up study. Laser-machined surfaces have a distinct colour appearance at visible spectral range. Colour indexing can be used for *in situ* monitoring of laser-machined workpieces and provides feedback for fully automated laser processing.

Author Contributions: Conceptualization, R.B., H-H.H., S.J.; methodology, R.B., H-H.H., N.Z., T.K.; software, R.B., M.K., T.K.; validation, N.Z., D.S., S.P., P.R.S.; formal analysis, N.Z., R.B.; investigation, N.Z.; resources, P.R.S.; data curation, R.B., N.Z.; writing—original draft preparation, S.J., N.Z., H-H.H.; writing—review and editing, all the authors; visualization, N.Z., S.J.; supervision, R.B.; project administration, R.B.; funding acquisition, R.B., P.R.S. All authors have read and agreed to the published version of the manuscript.

Funding: This research was partly funded by the Australian Research Council Linkage LP220100153 and Discovery DP240103231 grants.

Data Availability Statement: All the data are presented within this manuscript.

Acknowledgments: We acknowledge support by Swinburne University of Technology for lab allocation to test 80 W fs-laser machining system.

Conflicts of Interest: The authors declare no conflicts of interest.

Appendix A Tunnelling Ionisation

The atomic intensity $I_a = \varepsilon_0 c E_a^2/2 = 3.51 \times 10^{16}$ W/cm^2 corresponds to the electrical field strength $E_a = \frac{e}{4\pi\varepsilon_0 a_B^2} = 5.1 \times 10^9$ V/m at the electron orbit of the Bohr radius $a_B = \frac{\hbar^2}{m_e e^2} = 0.53$ Å in Hydrogen atom [35–37]. At laser intensity $I_L \geq I_a$, tunnelling ionisation dominates. This condition is defined by the Keldysh parameter $\gamma_K \equiv \omega_L \sqrt{2E_{ion}/I_L} < 1$, where ω_L is the cyclic frequency of laser and E_{ion} is the ionisation potential. When the external electrical field of strength E_{ex} is applied to an atom, the potential is given by $V(x) = -\frac{Ze^2}{x} - eE_{ex}x$ along the x direction. From the condition $\frac{dV(x)}{dx} = 0$, the position of barrier is $x_{max} = Ze/E_{ex}$, where Z is the atomic number (nuclear charge number). By setting $V(x_{max}) = E_{ion}$, the critical (threshold) field strength for barrier suppression ionisation (tunnelling) is obtained $E_c = \frac{E_{ion}^2}{4Ze^3}$. The corresponding laser intensity defines the *appearance intensity* for the ion in charge Z state, i.e., $I_{app} = cE_c^2/(8\pi) = \frac{cE_{ion}^4}{128\pi Z^2 e^6} = 4 \times 10^9 \left[\frac{E_{ion}}{[\mathrm{eV}]}\right]^4 Z^{-2}$ W/cm^2. For the H$^+$ ion with $E_{ion} = 13.61$ eV, $I_{app} = 1.4 \times 10^{14}$ W/cm^2, for Xe$^+$ with 12.13 eV: 8.6×10^{13} W/cm^2, for C$^+$ with 11.2 eV: 6.4×10^{13} W/cm^2 [38,39]. Hence, for the Hydrogen, which is used to define the *atomic intensity* I_a, the *appearance intensity* I_{app} of H$^+$ is only 0.4% of I_a. Interestingly, the ionisation threshold intensity was always higher for the circularly polarized light as compared with linearly polarised irradiation [38]. This is consistent with molecular alignment using two-pulse ionisation [40].

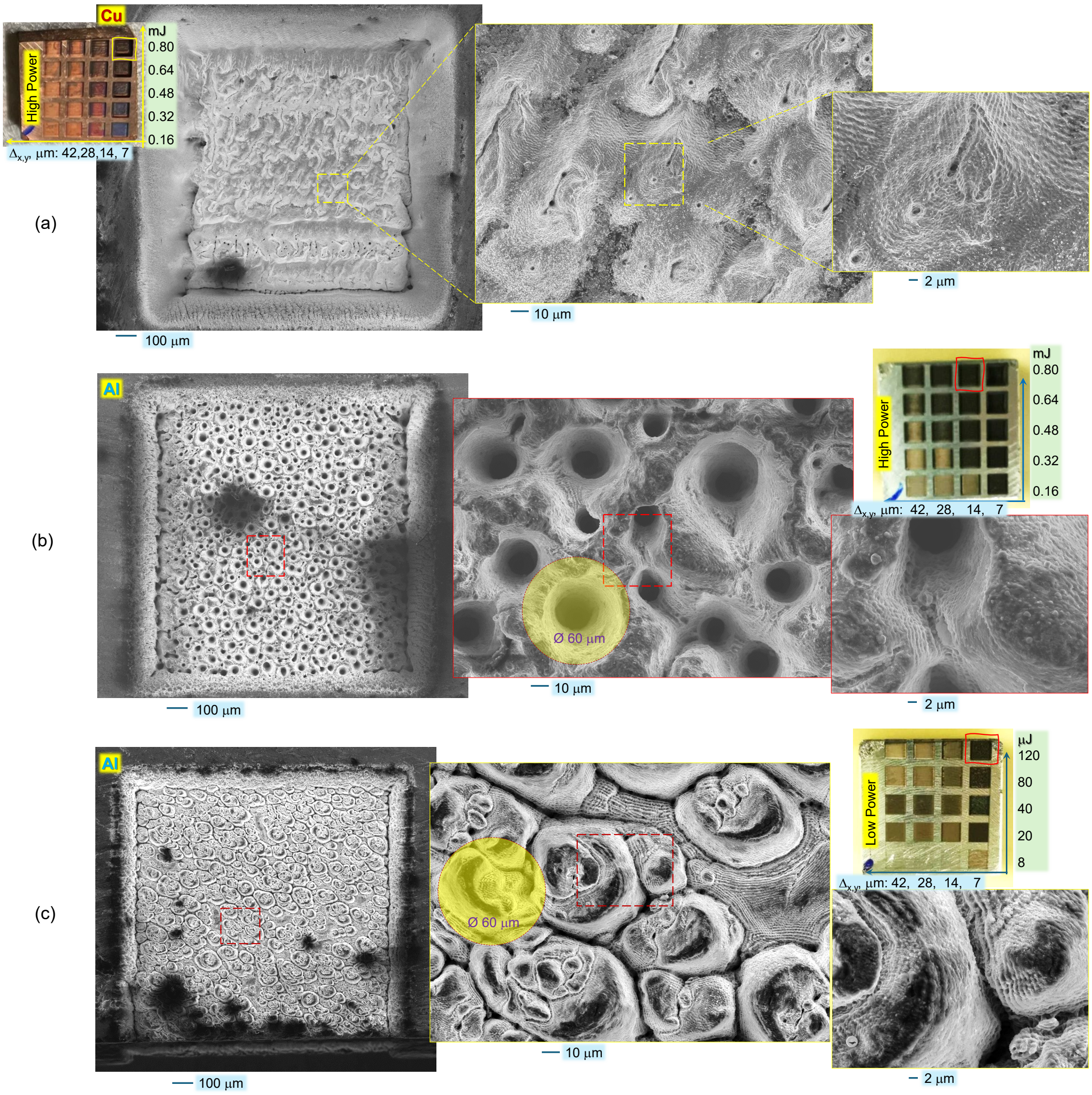

Figure A1. SEM images of characteristic examples of Cu and Al ablated by 1030 nm/200 fs/0.1 MHz irradiation at different scanning speeds corresponding to different in-line separation between pulses Δx and different pulse energies E_p. The focal spot size is $\sim 60\ \mu$m. Insets show optical images of Cu and Al coupons. Polarisation on the sample is close to circular (reflections on galvano-mirrors are making it slightly elliptical).

Appendix B Permittivity of Conductive Materials

The other popular definition of permittivity of conductive materials (semiconductors and metals) is defined as $\varepsilon' = \varepsilon'_1 - i\frac{4\pi\sigma}{\omega}$ [41], where σ is the conductivity and $\omega = 2\pi\nu = 2\pi c/\lambda$ is cyclic frequency of light (primed version of the same parameters as used in the main text is defined for distinction, e.g., the real part of permittivity is here ε'_1). Then, the complex refractive index $\tilde{n}' = n'(1 - i\kappa')$. With this definition, one can find useful expression to link optical and electrical (free electron) responses from $\varepsilon' = \tilde{n}'^2$: $\varepsilon'_1 = n'^2(1+\kappa')^2$ for the real part and $n'^2\kappa' = \frac{2\pi\sigma}{\omega} = \frac{\sigma}{\nu}$ (from the imaginary part of the refractive index). This section above shows the importance of the expressions used for the complex refractive indices: $(n + i\kappa)$ vs $n'(1 - i\kappa')$; the former is used in our analysis (not-primed). In the primed notations (n', κ') for $\lambda = 600$ nm: Cu $0.62(1 - i4.15)$ and Al $1.44(1 - i3.63)$.

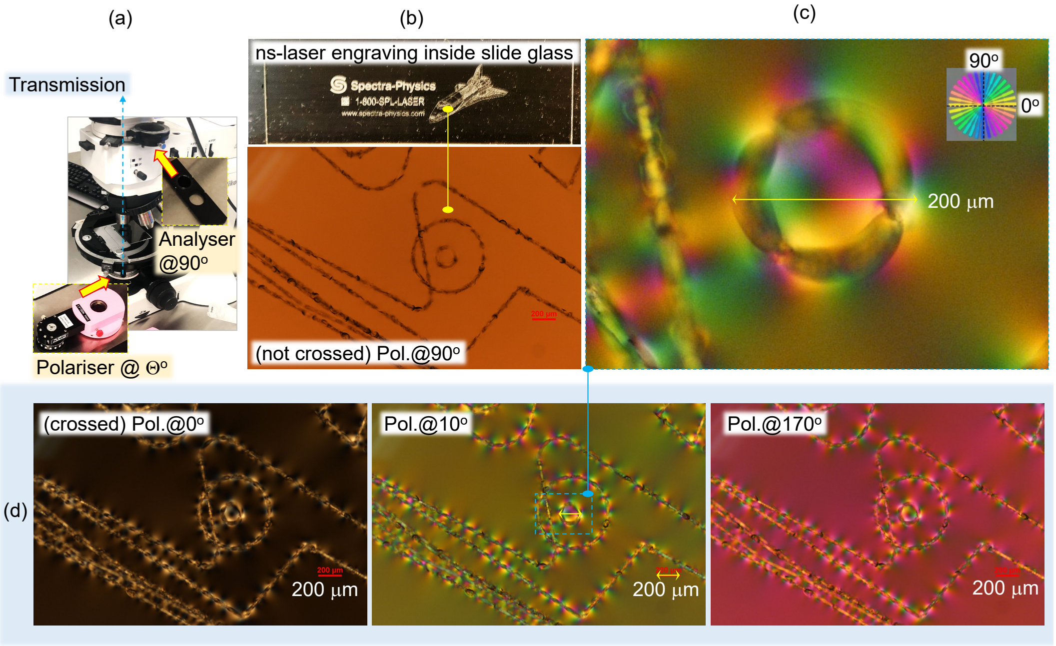

Figure A2. (a) Polychromatic polarization microscope (PPM) based on Nikon Optiphot with circular polariser-analyser units for transmission geometry. Polarisers are based on the optical activity (a birefringence for the circularly polarised light). (b) Optical images of a slide-glass with ns-laser (Hippo, Spectra Physics) engraved pattern [42] (courtesy Dr. M. Li). (c) Closeup view of the $\sim 200-\mu$m-diameter circular structure using PPM. (d) PPM images at different settings of the analyser orientation; $\theta = 0^\circ$ corresponds to the cross-Nikol condition.

The permittivity (epsilon) is linked to the (n', κ') via [41]:

$$n'^2 = \frac{1}{2}\left[\sqrt{\varepsilon'^2_1 + (2\sigma/\nu)^2} + \varepsilon'_1\right]; \quad n'^2\kappa'^2 = \frac{1}{2}\left[\sqrt{\varepsilon'^2_1 + (2\sigma/\nu)^2} - \varepsilon'_1\right]. \tag{A1}$$

For good conductors, when σ can be assumed frequency-independent and equal to the dc conductivity, the Hagen–Rubens relation can be used $R \approx 1 - 2\sqrt{2\varepsilon_0\omega/\sigma}$.

Appendix C Ablated Textures on Metals

Figure A1 shows characteristic examples of laser-ablated Cu and Al at high fluence. While the surface of Cu (melting $T_m = 1085^\circ$C) had a typically uneven surface at the bottom of the laser-ablated square box area (Figure A1(a)), there were no significant structural differences between regions ablated at different pulse energies and pulse overlap. In contrast, other patterns were observed on the surface of Al (melting $T_m = 660^\circ$C) dependent on the pulse energy and overlap (Figure A1(b,c)). At lower pulse energies $E_p \sim 0.1$ mJ (c), the ablated surface had a pattern of hillocks with a footprint area of tens-of-micrometers in cross-section. A clear light diffraction/interference pattern is recognizable on the ablated 3D surfaces. This indicates that surface formation by ablation rather than hydrodynamic flows induced by surface tension governed the surface pattern. When $E_p > 0.5$ mJ, a typical pit structure formed (b) with a density of holes dependent on the pulse overlap (b). The surface was not dominated by molten flows even at higher irradiance. This is unique to short-pulse laser ablation. The feature size of conical holes (b) is close to the full width at half maximum (FWHM) measure of the focal spot size. It is instructive to estimate the photon pressure exerted by a pulse of irradiance $I_p = 0.1$ PW/cm^2 or 10^{18} W/m^2: $P_{ph} = I_p/c \approx \frac{1}{3} \times 10^{10}$ Pa = 3.3 GPa, where $c \approx 3 \times 10^8$ m/s is speed of light. This pressure is applied when the fs-laser pulse energy is deposited (absorbed), while reflection doubles the momentum transfer, hence, pressure, due to the reversal of photon direction.

When pulse overlap was large 95-75% of focal diameter between the adjacent pulses at a ~ 0.1 MHz repetition rate and when heat accumulation is not prominent, the formation of deep conical pits is partly due to high-pressure application to softened/molten Al (Cu with higher melting temperature was not exhibiting this surface morphology). Such pits were more abundant in the regions of laser over-exposure at the turning points of the laser scan (change of direction). The ablation pressure has to be calculated considering laser ablation plasma conditions (temperature), however, the momentum conservation argument used for the above estimation is predicting high pressure $1 - 5$ GPa application onto the surface of ablated metals. This is promising for the laser peening applications [43]. The texture of ablated surfaces is qualitatively analysed here without deep studies in chemical modifications and residual stress which can be assessed from X-ray photo-electron spectroscopy (XPS) and X-ray diffraction (XRD), which are planned for the next stage of the study.

Appendix D Polarisation Analysis

Visualization of stress inside laser-processed regions inside dielectric materials (glasses and crystals) is usually visualized using a crossed-Nikol setup with an analyser-polariser for linear polarisation. By using a circularly polarised setup based on optical activity, there is the indifference of orientation for visualization of stress-induced birefringence (Figure A2); in the case of linear polarisers, orientation of stress should be at 45° with respect to the slow/fast axis of polarisers for highest contrast. Marking traces inscribed with ns-laser pulses have strong stress-induced birefringence around them.

References

1. Ng, S.H.; Han, M.; Hyde, L.; Durandet, Y.; Katkus, T.; Zaccaria, R.P.; Juodkazis, S. High Intensity Laser Applications: Space Prospective. 2021, number 12, pp. 2670–2677.
2. Mack, C.A. Will stochastics be the ultimate limiter for nanopatterning? Novel Patterning Technologies for Semiconductors, 2019, Vol. 10958, pp. 1095803,1–7.
3. Malinauskas, M.; Žukauskas, A.; Hasegawa, S.; Hayasaki, Y.; Mizeikis, V.; Buividas, R.; Juodkazis, S. Ultrafast laser processing of materials: from science to industry. *Light: Science & Applications* **2016**, *5*, e16133.
4. Jain, K.; Dunn, T.J.; Farmiga, N.; Zemel, M.; Weisbecker, C. Large-area high-throughput high-resolution lithography systems for flat-panel displays and microelectronic modules. Emerging Lithographic Technologies II, 1998, Vol. 3331, pp. 197–206.
5. McKee, D.C.; Bandera, C. Multistage foveal target detection system. Signal Processing, Sensor Fusion, and Target Recognition VII, 1998, Vol. 3374, pp. 194–203.
6. Jia, W.; Leung, Y.S.; Mao, H.; Xu, H.; Zhou, C.; Chen, Y. Hybrid-Light-Source Stereolithography for Fabricating Macro-Objects With Micro-Textures. *Journal of Manufacturing Science and Engineering* **2021**, *144*.
7. Maksimovic, J.; Hu, J.; Ng, S.H.; Katkus, T.; Seniutinas, G.; Rivera, T.P.; Stuiber, M.; Nishijima, Y.; John, S.; Juodkazis, S. Beyond Lambertian light trapping for large-area silicon solar cells: Fabrication methods. *Opto-Electronic Advances* **2022**, *5*, 210086–1.
8. Hilfiker, J.N.; Singh, B.; Synowicki, R.A.; Bungay, C.L. Optical characterization in the vacuum ultraviolet with variable angle spectroscopic ellipsometry: 157 nm and below. Vol. 3998, pp. 390–398.
9. Kitayama, T.; Itoga, K.; Watanabe, Y.; Uzawa, S. Proposal for a 50 nm proximity x-ray lithography system and extension to 35 nm by resist material selection. *Journal of Vacuum Science & Technology B: Microelectronics and Nanometer Structures Processing, Measurement, and Phenomena* **2000**, *18*, 2950–2954.
10. Rothschild, M.; Bloomstein, T.M.; Efremow, N.; Fedynyshyn, T.H.; Fritze, M.; Pottebaum, I.; Switkes, M. Nanopatterning with UV Optical Lithography. *MRS Bulletin* **2005**, *30*, 942–946.
11. Kozawa, T.; Tagawa, S. Radiation Chemistry in Chemically Amplified Resists. *Japanese Journal of Applied Physics* **2010**, *49*, 030001.
12. Hua, J.G.; Ren, H.; Huang, J.; Luan, M.L.; Chen, Q.D.; Juodkazis, S.; Sun, H.B. Laser-Induced Cavitation-Assisted True 3D Nano-Sculpturing of Hard Materials. *Small* **2023**, *19*, 2207968.
13. Žemaitis, A.; Gaidys, M.; Brikas, M.; Gečys, P.; Račiukaitis, G.; Gedvilas, M. Advanced laser scanning for highly-efficient ablation and ultrafast surface structuring: experiment and model. *Sci Rep* **2018**, *8*, 17376.

14. Buividas, R.; Mikutis, M.; Juodkazis, S. Surface and bulk structuring of materials by ripples with long and short laser pulses: Recent advances. *Progress in Quantum Electronics* **2014**, *38*, 119–156.
15. Wang, L.; Chen, Q.D.; Cao, X.W.; Buividas, R.; Wang, X.; Juodkazis, S.; Sun, H.B. Plasmonic nano-printing: large-area nanoscale energy deposition for efficient surface texturing. *Light: Science & Applications* **2017**, *6*, e17112–e17112.
16. Maksimovic, J.; Mu, H.; Han, M.; Smith, D.; Katkus, T.; Anand, V.; Nishijima, Y.; Ng, S.H.; Juodkazis, S. Si-Cr Nano-Alloys Fabricated by Direct Femtosecond Laser Writing. *Materials* **2023**, *16*, 1917.
17. Kerse, C.; Kalaycıoğlu, H.; Elahi, P.; Çetin, B.; Kesim, D.K.; Akçaalan, O.; Yavaş, S.; Aşık, M.D.; Öktem, B.; Hoogland, H.; Holzwarth, R.; Ilday, F.O. Ablation-cooled material removal with ultrafast bursts of pulses. *Nature* **2016**, *537*, 84–88.
18. Khurgin, J. Energy and Power Requirements for Alteration of the Refractive Index. *Light: Science & Applications* **2024**, *18*, 2300836.
19. Marlow, F.; Josten, S.; Leiting, S. Electronics with stainless steel: The work functions. *Journal of Applied Physics* **2023**, *133*, 085104.
20. Gamaly, E.G.; Rode, A.V.; Luther-Davies, B. Ablation of solids by femtosecond lasers: Ablation mechanism and ablation thresholds for metals and dielectrics. *Physics of Plasmas* **2002**, *18*, 949 – 957.
21. Juodkazis, S.; Okuno, H.; Kujime, N.; Matsuo, S.; Misawa, H. Hole Drilling in Stainless Steel and Silicon by Femtosecond Pulses at Low Pressure. *Appl. Phys. A* **2004 (DOI: 10.1007/s00339-004-2846-0)**, *79*, 1555 – 1559.
22. Jonušauskas, L.; Gailevičius, D.; Rekštytė, S.; Baldacchini, T.; Juodkazis, S.; Malinauskas, M. Mesoscale laser 3D printing. *Opt. Express* **2019**, *27*, 15205–15221.
23. Liu, J.M. Simple technique for measurements of pulsed Gaussian-beam spot sizes. *Opt. Lett.* **1982**, *7*, 196–198.
24. Gamaly, E.G.; Madsen, N.R.; Duering, M.; Rode, A.V.; Kolev, V.Z.; Luther-Davies, B. Ablation of metals with picosecond laser pulses: Evidence of long-lived nonequilibrium conditions at the surface. *Phys. Rev. B* **2005**, *71*, 174405.
25. Vanagas, E.; Kudryashov, I.; Tuzhilin, D.; Juodkazis, S.; Matsuo, S.; Misawa, H. Surface nanostructuring of borosilicate glass by femtosecond nJ energy pulses. *Appl. Phys. Lett.* **2003**, *82*, 2901–2903.
26. Vanagas, E.; Kawai, J.; Tuzilin, D.; Kudryashov, I.; Mizuyama, A.; Nakamura, K.G.; Kondo, K.I.; Koshihara, S.Y.; Takesada, M.; Matsuda, K.; Juodkazis, S.; Jarutis, V.; Matsuo, S.; Misawa, H. Glass cutting by femtosecond pulsed irradiation. *J. Microlith. Microfab. Microsyst.* **2004**, *3*, 358–363.
27. Kretkowski, M.; Jabłoński, R.; Shimodaira, Y. Development of an XYZ Digital Camera with Embedded Color Calibration System for Accurate Color Acquisition. *IEICE Transactions on Information and Systems* **2010**, *E93.D*, 651–653.
28. Kretkowski, M.; Shimodaira, Y.; Jabłoński, R. Color calibration method providing uniform distribution of color difference throughout the whole vision gamut. *Journal of Automation, Mobile Robotics and Intelligent Systems* **2013**, *3*, 213–216.
29. Jia, R.; Xiang, S.; Wang, Y.; Chen, H.; Xiao, M. Electrically Triggered Color-Changing Materials: Mechanisms, Performances, and Applications. *Advanced Optical Materials* **2024**, *12*, 2302222.
30. Tian, B.; Wang, Z.; Smith, A.T.; Bai, Y.; Li, J.; Zhang, N.; Xue, Z.; Sun, L. Stress-induced color manipulation of mechanoluminescent elastomer for visualized mechanics sensing. *Nano Energy* **2021**, *83*, 105860.
31. Greffet, J.J.; Nieto-Vesperinas, M. Field theory for generalized bidirectional reflectivity: derivation of Helmholtz's reciprocity principle and Kirchhoff's law. *15*, 2735–2744.
32. Greffet, J.J.; Carminati, R.; Joulain, K.; Mulet, J.P.; Mainguy, S.; Chen, Y. Coherent emission of light by thermal sources. *416*, 61–64.
33. Wang, X.; Seniutinas, G.; Balcytis, A.; Kasalynas, I.; Jakstas, V.; Janonis, V.; Venckevicius, R.; Buividas, R.; Appadoo, D.; Valusis, G.; others. Laser structuring for control of coupling between THz light and phonon modes. *arXiv preprint arXiv:1605.04493* **2016**.
34. Nishijima, Y.; Balčytis, A.; Naganuma, S.; Seniutinas, G.; Juodkazis, S. Kirchhoff's metasurfaces towards efficient photo-thermal energy conversion. *Scientific Reports*, *9*, 8284.
35. Gibbon, P. Introduction to Plasma Physics. Vol. CERN-2016-001; the Proceedings of the CAS-CERN Accelerator School: Plasma Wake Acceleration, 23–29 Nov. 2014, Geneva, Switzerland, pp. 51–65.
36. Gibbon, P.; Förster, E. Short-pulse laser - plasma interactions. *Plasma Physics and Controlled Fusion* **1996**, *38*, 769–793.
37. Gibbon, P. *Short pulse laser interactions with matter: an introduction*; World Scientific, 2005.

38. Auguste, T.; Monot, P.; Lompre, L.; Mainfray, G.; Manus, C. Multiply charged ions produced in noble gases by a 1 ps laser pulse at λ = 1053 nm. *I. Phys. B: At. Mol. Opt. Phys.* **1992**, *25*, 4181–4194.
39. Gibbon, P. Physics of High Intensity Laser Plasma Interactions, 2011. Varenna Summer School on Laser-Plasma Acceleration 20–25 June 2011.
40. Normand, D.; Lompre, L.; Comaggia, C. Laser-induced molecular alignment probed by a double-pulse experiment. *I. Phys. B: At. Mol. Opt. Phys.* **1992**, *25*, L497–L503.
41. Collett, E. *Field guide to Polarisation*; SPIE Press, Bellingham, Washington USA, 2005.
42. Vanagas, E.; Ye, J.Y.; Li, M.; Miwa, M.; Juodkazis, S.; Misawa, H. Analysis of stress induced by a three-dimensional recording in glass. *Appl. Phys. A* **2005**, *81*, 725 – 727.
43. Zhou, L.; Li, X.Y.; Zhu, W.J.; Wang, J.X.; Tang, C.J. The effects of pulse duration on ablation pressure driven by laser radiation. *Journal of Applied Physics* **2015**, *117*, 125904.